19. Lidzey, D. G. *et al.* Strong exciton–photon coupling in an organic semiconductor microcavity. *Nature* **395,** 53–56 (1998).
20. Lidzey, D. G., Bradley, D. D. C., Armitage, A., Walker, S. & Skolnick, M. S. Photon-mediated hybridisation of Frenkel excitons in organic semiconductor microcavities. *Science* **288,** 1620–1623 (2000).

Acknowledgements

We thank U. Oesterle and R. Houdré for growing the InGaAs sample, and J.D. Ganiere, G. Hayes, A. Quattropani, R. Romestain, P. Senellart and P. Schwendimann for suggestions. This work has been supported in part by the Fonds National Suisse de la Recherche Scientifique.

Correspondence and requests for materials should be addressed to M.S. (e-mail: Michele.Saba@epfl.ch).

Hierarchical self-assembly of metal nanostructures on diblock copolymer scaffolds

Ward A. Lopes*† & Heinrich M. Jaeger*

* *James Franck Institute and Department of Physics, The University of Chicago, Chicago, Illinois 60637, USA*

Self-assembly is emerging as an elegant, 'bottom-up' method for fabricating nanostructured materials[1–8]. This approach becomes particularly powerful when the ease and control offered by the self-assembly of organic components is combined with the electronic, magnetic or photonic properties of inorganic components[2,5,9]. Here we demonstrate a versatile hierarchical approach for the assembly of organic–inorganic, copolymer–metal nanostructures in which one level of self-assembly guides the next. In a first step, ultrathin diblock copolymer films form a regular scaffold of highly anisotropic, stripe-like domains[10–12]. During a second assembly step, differential wetting guides diffusing metal atoms to aggregate selectively along the scaffold, producing highly organized metal nanostructures. We find that, in contrast to the usual requirement of near-equilibrium conditions for ordering[2,3,13], the metal arranged on the copolymer scaffold produces the most highly ordered configurations when the system is far from equilibrium. We delineate two distinct assembly modes of the metal component—chains of separate nanoparticles and continuous wires—each characterized by different ordering kinetics and strikingly different current–voltage characteristics. These results therefore demonstrate the possibility of guided, large-scale assembly of laterally nanostructured systems.

Two important, competing, issues for the assembly of inorganic materials on organic scaffolds are high density and selectivity. In the case of scaffolds formed by copolymer domains (Fig. 1), preferential wetting of one of the copolymer blocks by metal will selectively aggregate the metal inside the corresponding domain[14,15]. However, simple coalescence of dense metal nanoparticle aggregates into the overall shape given by the boundaries of the selected copolymer domain—similar to that observed for water droplets filling out a narrow hydrophilic strip[3]—has not been achieved so far. This is because of the large surface energies of metals, exceeding those of copolymers by orders of magnitude. Consequently, metal–metal bonds will overwhelm metal–polymer bonds and, except for very small metal concentrations, the final configuration will be a large, spherical metal aggregate that completely ignores the polymer scaffold and mitigates selectivity. Thus, under equilibrium conditions even highly elongated, anisotropic polymer scaffolds may not be able to guide self-assembling metal particles into wire-like nanostructures. But here we show how non-equilibrium processes can induce, and stabilize, recognition of complex patterns provided by a nanoscale scaffold.

The particular, asymmetric polystyrene-block-poly(methylmethacrylate) (PS-b-PMMA) diblock copolymer that we used forms parallel cylindrical domains of PMMA, with a repeat spacing of 50 nm, surrounded by PS. Sample fabrication followed a two-level self-assembly process. First, spin-casting of the copolymer from solution to a thickness equivalent to one repeat spacing, and subsequent annealing, produced a thin film consisting of laterally alternating domains[11,12] (Fig. 1). Control over the domain curvature and orientation is possible, for example by applied in-plane electric fields[10,16], but was not the focus of the work described here. Instead, we consider the copolymer domain pattern as a given scaffold, and focus on the second assembly step, in which a small amount of metal (of nominal thickness 0.5–12 nm) was thermally evaporated onto the copolymer film, and the metal atoms were allowed to diffuse[17,18]. During this second step, the template morphology does not change as long as the molecular mass is sufficiently high that the order–disorder temperature is not reached[10].

For a wide range of metals and small deposited amounts (film thickness typically < 0.6 nm, depending on the metal and the deposition rate), selective decoration of one of the two copolymer domains is already apparent immediately after metal deposition (Fig. 2a). We observed this behaviour for Au, Ag, In, Pb, Sn and Bi, with Au and Ag preferring the PS domain, and In, Pb, Sn and Bi the PMMA domain. In each of these cases, the preferred domain becomes the scaffold. Selectivity of nearly 100% is achieved by warming the system in an inert gas atmosphere to a temperature that is above the copolymer glass temperature, but below the point at which the template pattern disintegrates (< 300 °C for PS-b-PMMA) (Fig. 2b). Inside the preferred domain, this leads to a coarsening that increases both the size and the separation of the nanoparticles while the metal also diffuses into the domains, perpendicular to the film plane[18,19]. With the exception of Ag, depositing larger amounts of metal does not fill out the domains. Rather than coalescing into continuous, elongated structures of high aspect ratio, the material ignores the template and 'jumps the

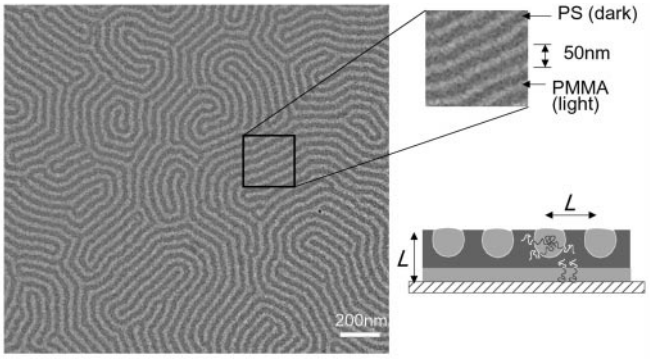

Figure 1 Transmission electron microscopy (TEM) image of ultrathin diblock copolymer film. The PS-b-PMMA copolymer (total molecular mass, 84,000; PS molecular mass, 60,000; polydispersity, 1.08; Soxhlet-extracted with cyclohexane to remove excess homopolymer PS in the diblock copolymer as obtained from Polysciences, Inc.) was spin-cast from solution to obtain a film thickness corresponding to the bulk repeat spacing, *L*. Spin-casting onto amorphous Si_3N_4 membrane substrates[25] allowed direct investigation by TEM without sample removal. The sketch shows a cross-section of the resulting film morphology. The striped domain pattern spontaneously forms as a consequence of phase separation between the two copolymer blocks, and provides the first level in a hierarchy of self-assembly levels. Image contrast results from electron-beam irradiation-thinning of the PMMA domains, which therefore appear lighter.

† Present address: Arryx Inc., 316 N. Michigan Avenue, Suite CL20, Chicago, Illinois 60601, USA.

© 2001 Macmillan Magazines Ltd

gap' between neighbouring domains. Subsequent annealing only reduces the aspect ratio and leads to particles that are more like spheres, but does not reinstate selectivity. These results make it clear that high-density, selective metal decoration cannot result from equilibrium states of the metal–copolymer system.

One path to increased metal density is to use repeated deposition and short-time annealing of small amounts of metal. This is equivalent to generating a large number of nucleation sites for metal droplet formation inside the preferred domains, while limiting nanoparticle coalescence by keeping the coarsening far from the final, equilibrium state. This approach produces dense nanochains (Fig. 2c) of fairly narrow particle size distribution. A second possibility utilizing non-equilibrium behaviour involves tailoring the metal–polymer interactions such that, at least over some time window, the metal effectively wets one of the two copolymer domains but de-wets the other. This requires a very high mobility contrast between the two copolymer domains, allowing the metal to clear one domain and aggregate at high volume fraction in the other before surface tension drives the aggregate into its final, spherical shape. However, under a wide range of conditions (deposition of films up to 15 nm thick at rates from 0.01 to 1 nm s^{-1}), we never found Au, In, Pb, Sn or Bi to fully wet their preferred domain during any part of the self-assembly process. At best, we observed ellipsoids with aspect ratios of no more than 4–5 for Au.

The exception is silver, which exhibits behaviour very different from all the other metals that we investigated and, at coverages >10 nm, easily forms continuous nanowires along the PS domains (Fig. 2d and e). The extremely high surface mobility of Ag on PMMA is apparent from the fact that no annealing is required to produce essentially 100% selectivity (Fig. 2e). Changes in the rate of metal deposition did not qualitatively affect wire formation or selectivity. Note that these wires can follow the 25-nm-wide polymer scaffolds over distances of micrometres without breaks. Once formed, the wires were stable for at least 9 months at room temperature. Yet with a surface tension for Ag of around 1.2–1.4 J m^{-2} (ref. 20), three orders of magnitude higher than that for the polymers[21], and with the silver–silver interaction known to dom-

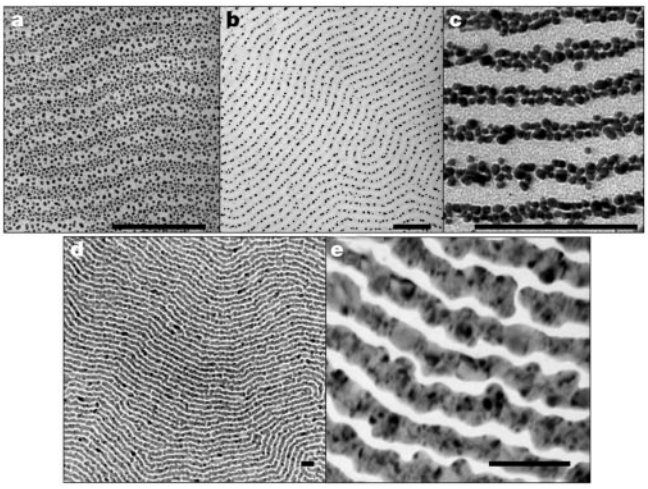

Figure 2 Metal nanochain and nanowire formation on PS-*b*-PMMA at different stages during the second self-assembly level. **a**, Aggregation of Au metal, vapour-deposited onto copolymer film (3 nm nominal metal film thickness), into nanometre-sized islands. Before annealing, the difference in wetting properties between the two copolymer domains is already apparent. **b**, Annealing at 180 °C for 1 min in an Ar atmosphere produces highly selective Au decoration of the PS domains. Inside the preferred domains (the scaffold), the metal forms chains of nanoparticles. **c**, Repeated deposition and short-time annealing (3×2 nm / 180 °C) leads to densely packed nanochains. With this procedure, PS domains can be loaded with metal nanoparticles to volume fractions exceeding 30% without incurring more than 10 metal bridges per square micrometre between neighbouring PS regions. Qualitatively similar results are obtained for In, Sn, Pb or Bi. **d**, Large-scale TEM micrograph, and **e**, close-up view of self-assembled Ag nanowires. Nominally 12-nm Ag was deposited onto the copolymer film without subsequent annealing. Note the extreme mobility and selectivity of Ag. Ag prefers the PS domains (see also Fig. 3b). Smaller deposited amounts of Ag (<3 nm) show the same high selectivity, but assemble into nanochains as in **b**. Individual nanocrystallites inside the wires exhibit varying grey levels owing to Bragg scattering from differently oriented lattice planes. All metal depositions were performed at base pressures of $(1-2)\times10^{-6}$ torr and rates of 0.005–0.1 nm s^{-1}. Scale bars: 200 nm in **a**–**c**, and 100 nm in **d** and **e**.

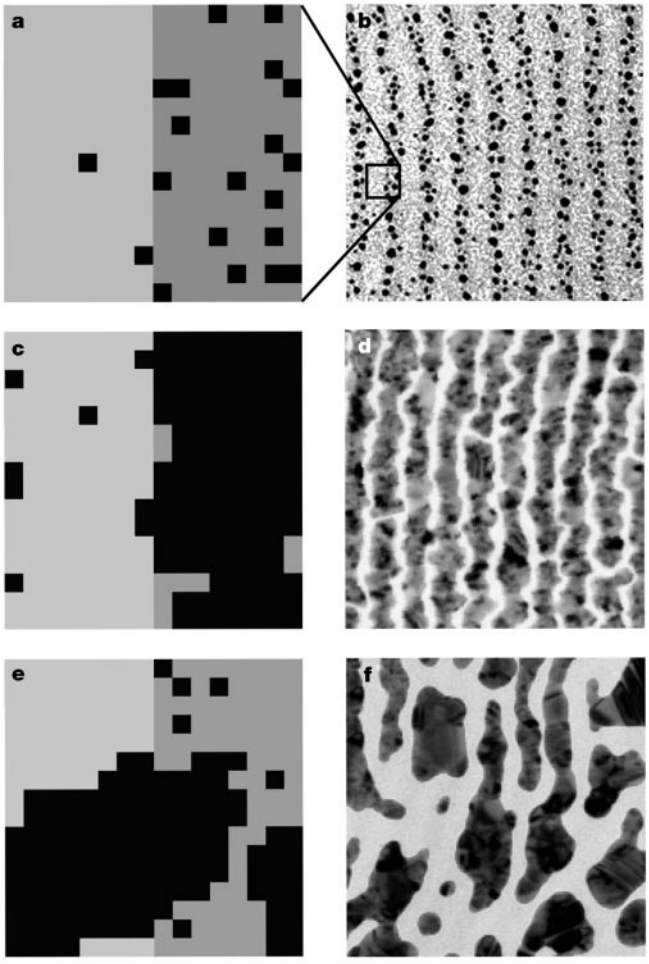

Figure 3 Comparison of Monte Carlo simulation (left column) and experimental results (right column) for Ag nanowire formation. The simulation results shown were obtained for mobility ratio $m \ll 1$ and sticking coefficient $0.8 < S < 1$. **a**, **b**, Early stages of metal diffusion and aggregation after 20 out of a total of 128 random walkers have been started in the simulation, or about 2 nm of Ag has been deposited in the experiment. The simulation considers diffusion and aggregation on a lattice consisting of a high- and a low-mobility side, coloured light and dark grey, respectively. The aggregation of Ag atoms into well separated nanoparticles with typical diameters around 10 nm inside the polystyrene domains, corresponding to the darker regions in the TEM micrograph, is seen in **b** and replicated in **a**. **c**, **d**, Once all 128 walkers have been randomly added to the simulation, highly domain-selective aggregation into continuous wire-like nanostructures completely fills the low-mobility side of the lattice. In the experiment, this corresponds to deposition of >12 nm Ag. **e**, **f**, At later stages in the simulation (**e**), the highly anisotropic, elongated wires in **c** deform. This is mediated by a strong metal–metal interaction that allows for a high mobility of walkers along the perimeter of aggregates, negating the low mobility for diffusion on the underlying polymer and favouring rounded overall shapes. Qualitatively, the same tendency toward more spherical, equilibrium shapes is seen in the experiments if the system is warmed to >80 °C (**f**). Removal of the Ag by a suitable etch shows that only the metal deforms, while the underlying template retains its original morphology as in Fig. 1 (in the TEM micrograph (**f**), the comparatively low-contrast polymer domains are not discernible).

© 2001 Macmillan Magazines Ltd

inate over the Ag–PS interaction[22], the wires are clearly non-equilibrium structures: the equilibrium state for Ag on the diblock is of spherical shape, as for the other metals.

To elucidate the kinetic mechanism responsible for wire formation, we performed two-dimensional Monte Carlo simulations. Figure 3 compares snapshots from one such simulation with experimental results. The simulation involved 16×16 lattice sites with periodic boundary conditions to represent a $50\,\text{nm} \times 50\,\text{nm}$ 'unit cell' of the sample, containing one PMMA domain (light grey) and one PS domain (dark grey). Occupied sites on the lattice ('random walkers', black squares) representing Ag atoms or small Ag clusters were allowed to diffuse and aggregate over time. Approximating the way that the atoms land on the diblock template during metal deposition and the time that small clusters take to form, the simulation added individual walkers to the lattice gradually, but spatially randomly, until 50% of all available lattice sites were occupied. The ratio of the mobilities on the two halves of the lattice is $m \approx D_{PS}/D_{PMMA}$, where D_i is the metal diffusion constant for motion in copolymer domain i. The metal–metal interaction was modelled by an attractive interaction mediated by a sticking coefficient, S, and a hard-core repulsion to avoid particle overlap. The mobility of metal aggregates containing $N > 1$ neighbouring walkers was taken to vary as $1/N$. Because the metal prefers one of the copolymer domains (PS in the case of Ag or Au) over the other, even under equilibrium conditions, a small energy difference between the two halves of the lattice was included. This difference is insignificant, however, when compared to the attractive metal–metal interaction.

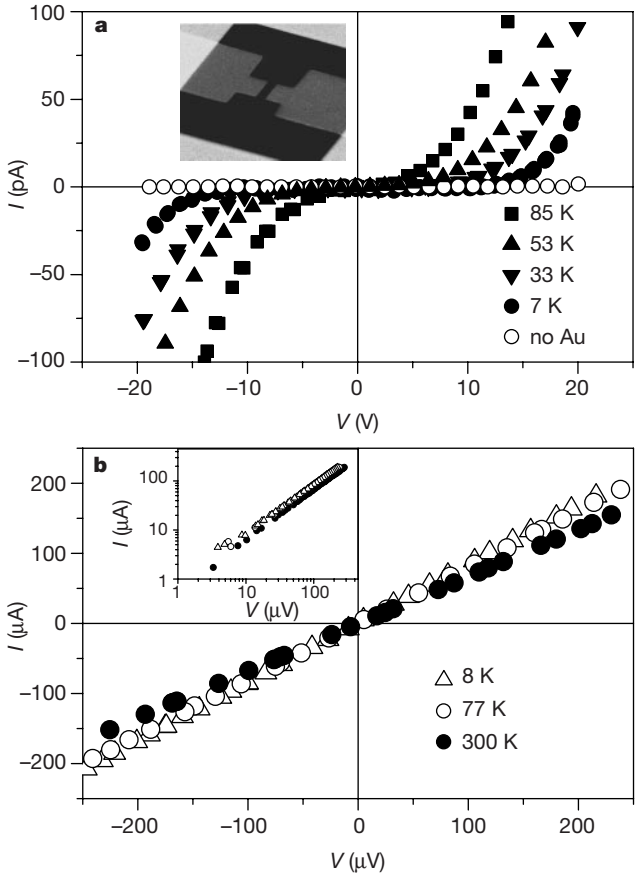

Figure 4 Electronic transport measurements on self-assembled nanochains (**a**) and nanowires (**b**). The samples were prepared on silicon nitride membrane substrates[25] which allowed for all self-assembly steps, as well as in-plane electrode fabrication, low-temperature transport measurements, and finally direct TEM observation to be performed on the same sample without removal from the substrate. The inset to **a** shows a scanning electron micrograph of the central region of the substrate (a membrane 100 nm thick, transparent to electrons and thus appearing dark) with 17-nm-thick Cr electrodes that were used both for copolymer domain alignment[16] during the first assembly level, and later to interface the nanochain array to external circuitry. **a**, The self-assembled copolymer scaffold, not yet decorated with Au nanoparticles, exhibits current levels < 50 fA across the in-plane electrodes (gap spacing 4 μm). After Au decoration (see Fig. 2c for a close-up of the sample), highly nonlinear current–voltage characteristics (I–V curves) are observed. The nonlinearity arises from large charging energies that at low bias voltages prevent electron tunnelling between nanoparticles embedded in the surrounding polystyrene matrix. The spread in nanoparticle sizes and spacings along the current paths inside each copolymer domain translates into a range of single-electron charging energies and tunnel resistances. At higher temperatures, additional paths involving smaller islands—that is, larger charging energies—become accessible and lead to an increased conductance, particularly at small bias voltages[26]. **b**, Metallically continuous Ag nanowires, by contrast, exhibit highly linear I–V curves. The inset shows that this ohmic behaviour extends down to the smallest voltage levels measured. This sample, shown close up in Fig. 2d and e, had 2-mm-wide in-plane electrodes, resulting in an array of $\sim 10^4$ parallel nanowires of which about 10% were continuous across the electrode gap (12 μm).

By a suitable choice of the two parameters m and S, we achieved a good correspondence between experiment and simulation (Fig. 3), including the early stages at very low metal coverage and the formation of continuous wires at intermediate times. Also apparent is the disintegration of these wires as the system comes closer to equilibrium. Experimentally, the self-assembled wire structures can be stabilized by quenching the sample after metal deposition (to room temperature in the case of Ag). Moderate warming to $> 80\,^{\circ}\text{C}$ changes the Ag wires into rounded shapes (Fig. 3f), which correspond well with the bulbous structures seen in the simulation at late stages (Fig. 3e). Close inspection by transmission electron microscopy (TEM) and diffraction measurements show that the Ag wires immediately after metal deposition (Fig. 3d) are highly polycrystalline, while a slight anneal induces a rapid growth of larger (tens of nanometres) single-crystalline regions before the wires disintegrate. This again demonstrates a very large surface mobility of Ag atoms, not only on PMMA but also on the Ag nanocrystallites.

Although a more quantitative comparison with experiment may require a more realistic model, the present simulation demonstrates the possibility of tailoring the copolymer + metal system to optimize wire formation. Exploration of the (m,S) parameter space shows[23] that this requires $m \to 0$ and $S \to 1$. As metal–metal bond energies E_b are large compared to the thermal energy, k_BT, near room temperature, the parameter $S = 1 - \exp[-E_b/(k_BT)]$ cannot deviate much from unity. However, m is affected by the choice of both copolymer and metal. From control experimentss[23] with Ag on homopolymer PS and PMMA of the same molecular masses as in the copolymer we estimate[23] $0.005 < m < 0.03$. Although we found such a value only for Ag, suitable metal alloys and different copolymers should provide a straightforward means for tuning m.

To demonstrate the versatility of this hierarchical route for self-assembly of functional, laterally nanostructured systems, we now discuss the distinctly different behaviour produced by the nanochains and nanowires shown in Fig. 2. At high metal-loading fractions, the particles come close enough to provide electrically conducting paths. Figure 4 shows electronic transport measurements obtained for fully self-assembled conductors of this type. Nanochains exhibit highly nonlinear current–voltage (I–V) curves (Fig. 4a), characteristic of single-electron tunnelling between nanometre-sized metal islands in the presence of strong charging (Coulomb blockade) effects[24]. The large overall threshold voltage for current onset results from the series combination of many such tunnel junctions along the current path. At low voltage bias, the structures are essentially insulating but switch over to conducting behaviour beyond the threshold. By contrast, the I–V curves for the nanowires are linear (Fig. 4b). Such ohmic response is indicative of continuous, metallic connections across the sample. The resistivity of a few μΩ cm (using TEM on the same sample to estimate the

© 2001 Macmillan Magazines Ltd

number and geometry of fully connected paths) is in line with the notion of grain-boundary-dominated transport in a polycrystalline metal, as is the observation of only a small decrease of the resistance with decreasing temperature. Thus, for a given overall geometry of conduction paths, controlled by the self-assembly of the copolymer scaffold, the ability to tune the metal–polymer kinetics of the second assembly level provides the flexibility to tailor the transport behaviour independently—and over the whole range from insulating or semiconducting to metallic.

This ability to separate, by hierarchical self-assembly, the formation of the organic scaffold from the processes functionalizing it with an inorganic component, in our case metal, opens up possibilities of assembling nanostructures with large anisotropy and very high local dielectric contrast, suitable for nanogratings, interconnects or sensor applications. Finally, although we have described a prototype hierarchical assembly process with two levels, additional levels are clearly possible. For example, the structures shown in Fig. 2 might form the basis for electroless plating steps or for the attachment of suitable biomolecules. □

Received 6 June; accepted 26 October 2001.

1. Boal, A. K. *et al.* Self-assembly of nanoparticles into structured spherical and network aggregates. *Nature* **404,** 746–748 (2000).
2. Black, C. T., Murray, C. B., Sandstrom, R. L. & Sun, S. Spin-dependent tunneling in self-assembled cobalt-nanocrystal superlattices. *Science* **290,** 1131–1134 (2000).
3. Gau, H., Herminghaus, S., Lenz, P. & Lipowsky, R. Liquid morphologies on structured surfaces: from microchannels to microchips. *Science* **283,** 46–49 (1999).
4. Higgins, A. M. & Jones, R. A.L. Anisotropic spinodal dewetting as a route to self-assembly of patterned surfaces. *Nature* **404,** 476–478 (2000).
5. Thurn-Albrecht, T. *et al.* Ultrahigh-density nanowire arrays grown in self-assembled diblock copolymer templates. *Science* **290,** 2126–2129 (2000).
6. Park, M., Harrison, C., Chaikin, P. M., Register, R. A. & Adamson, D. H. Block copolymer lithography: periodic arrays of ~10^{11} holes in 1 square centimeter. *Science* **276,** 1401–1404 (1997).
7. Spatz, J. P., Mössmer, S., Hartmann, C. & Möller, M. Ordered deposition of inorganic clusters from micellar block copolymer films. *Langmuir* **16,** 407–415 (2000).
8. Whitesides, G. M., Mathias, J. P. & Seto, C. T. Molecular self-assembly and nanochemistry: A chemical strategy for the synthesis of nanostructures. *Science* **254,** 1312–1319 (1991).
9. Sanchez, C. & Lebeau, B. Design and properties of hybrid organic-inorganic nanocomposites for photonics. *Mater. Res. Soc. Bull.* **26,** 377–387 (2001).
10. Fasolka, M. J. & Mayes, A. M. Block copolymer thin films: physics and applications. *Annu. Rev. Mater. Res.* **31,** 323–355 (2001).
11. Morkved, T. L. & Jaeger, H. M. Thickness-induced morphology changes in lamellar diblock copolymer ultrathin films. *Europhys. Lett.* **40,** 643–648 (1997).
12. Tang, W. H. & Witten, T. A. Quenched degrees of freedom in symmetric diblock copolymer thin films. *Macromolecules* **31,** 3130–3135 (1998).
13. Harrison, C. *et al.* Mechanisms of ordering in striped patterns. *Science* **290,** 1558–1560 (2001).
14. Balazs, A. C. Interactions of nanoscopic particles with phase-separating polymeric mixtures. *Curr. Opin. Colloid Interface Sci.* **4,** 443–448 (2000).
15. Morkved, T. L., Wiltzius, P., Jaeger, H. M., Grier, D. G. & Witten, T. A. Mesoscopic self-assembly of gold islands on diblock-copolymer films. *Appl. Phys. Lett.* **64,** 422–424 (1994).
16. Morkved, T. L. *et al.* Local control of microdomain orientation in diblock copolymer thin films with electric fields. *Science* **273,** 931–933 (1996).
17. Cole, D. H., Shull, K. R., Rehn, L. & Baldo, P. Metal-polymer interactions in a polymer/metal nanocomposite. *Phys. Rev. Lett.* **78,** 5006–5009 (1997).
18. Lin, B. *et al.* X-ray studies of polymer/gold nanocomposites. *J. Appl. Phys.* **85,** 3180–3184 (1999).
19. Guico, R. S., Richter, A. G., Wang, J. & Shull, K. R. X-ray standing wave measurements of gold nanoparticles in polymeric thin films. *Polymeric Materials: Science & Engineering (Abst.)* **85,** (American Chemical Society, Washington, in the press).
20. Piuz, F. & Borel, J. P. Thermodynamical size effect in small particles of silver. *Phys. Status Solidi A* **14,** 129–133 (1972).
21. Wu, S. *Polymer Interfaces and Adhesion* (Marcel Decker, New York, 1982).
22. Gerenser, L. J. & Goppert-Berarducci, K. E. in *Metallized Plastics 3: Fundamental and Applied Aspects* (ed. Mittal, K. L.) 163–178 (Plenum, New York, 1992).
23. Lopes, W. Non-equilibrium self-assembly of metals on diblock copolymer templates. *Phys. Rev. E* (submitted).
24. Ford, E. M. & Ahmed, H. Control of Coulomb blockade characteristics with dot size and density in planar metallic multiple tunnel junctions. *Appl. Phys. Lett.* **75,** 421–423 (1999).
25. Morkved, T. L., Lopes, W. A., Hahm, J., Sibener, S. J. & Jaeger, H. M. Silicon nitride membrane substrates for the investigation of local structure in polymer thin films. *Polymer* **39,** 3871–3875 (1998).
26. Cordan, A. S. *et al.* Temperature behavior of multiple tunnel junction devices based on disordered dot arrays. *J. Appl. Phys.* **87,** 345–352 (2000).

Acknowledgements

We thank T. Witten, S. Coppersmith, T. Morkved, M. Möller and K. Shull for discussions, and R. Parthasarathy for help with some of the *I–V* measurements. This work was supported by the MRSEC programme of the NSF and by the W. M. Keck Foundation.

Correspondence should be addressed to H.M.J.
(e-mail: h-jaeger@uchicago.edu).

Himalayan tectonics explained by extrusion of a low-viscosity crustal channel coupled to focused surface denudation

C. Beaumont*, R. A. Jamieson†, M. H. Nguyen*† & B. Lee*

** Department of Oceanography, Dalhousie University, Halifax, Nova Scotia, Canada, B3H 4J1*
† Department of Earth Sciences, Dalhousie University, Halifax, Nova Scotia, Canada, B3H 3J5

Recent interpretations of Himalayan–Tibetan tectonics have proposed that channel flow in the middle to lower crust can explain outward growth of the Tibetan plateau[1–3], and that ductile extrusion of high-grade metamorphic rocks between coeval normal- and thrust-sense shear zones can explain exhumation of the Greater Himalayan sequence[4–7]. Here we use coupled thermal–mechanical numerical models to show that these two processes—channel flow and ductile extrusion—may be dynamically linked through the effects of surface denudation focused at the edge of a plateau that is underlain by low-viscosity material. Our models provide an internally self-consistent explanation for many observed features of the Himalayan–Tibetan system[8–10].

Figure 1 shows a general cross-section, highlighting features of the orogen (numbers 1–9) requiring explanation in any quantitative model[10]. These include contemporaneous north–south shortening on the Main Central thrust (MCT) system (1) and extension along the South Tibetan detachment (STD) system (2), the creation of gneiss domes (3) in the southern Tibetan plateau, the style and timing of metamorphism in the Greater Himalayan (GHS, 5) and Lesser Himalayan (LHS, 6) sequences, and the juxtaposition of contrasting protoliths (8) across the MCT zone. We show below that these disparate observations can all be interpreted to result from coupling between channel flow originating in partially molten crust beneath Tibet (4) and rapid denudation of the south flank of the Himalaya (7).

We first present the behaviour of a reference model (model 1; Fig. 2), and demonstrate a similar tectonic style with boundary

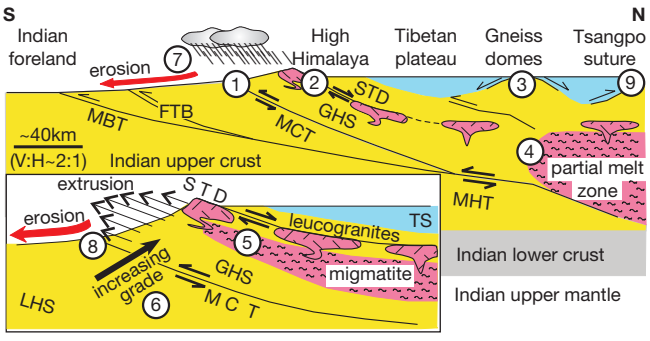

Figure 1 General tectonic features of the Himalaya and southern Tibet[5,8–10,15,16]. Numbers 1–9 correspond to important features requiring explanation[10]; see Figs 2–4 for corresponding features of models. Inset shows southern flank of Tibetan plateau (not to scale) with geological features discussed in text. LHS, Lesser Himalayan sequence; GHS, Greater Himalayan sequence; TS, Tethyan sequence; MCT, Main Central thrust; STD, South Tibetan detachment; MHT, Main Himalayan thrust; MBT, Main Boundary thrust; FTB, fold-thrust belt (Siwaliks). Colours (all figures): blue, weak upper crust; yellow, medium-strength middle crust; grey, strong lower crust; pink, melt-weakened middle crust (includes migmatite and plutons).

© 2001 Macmillan Magazines Ltd